JOURNAL OF AIRCRAFT
Vol. 34, No. 2, March–April 1997

Effects of Unsteady Aerodynamics on the Flight Dynamics of an Articulated Rotor Helicopter

Stephen Richard Turnour* and Roberto Celi†
University of Maryland, College Park, Maryland 20742

This paper presents the results of a study of the effects of unsteady airfoil aerodynamics on several flight dynamics characteristics of an articulated rotor helicopter. A new trim algorithm is presented that reduces the otherwise potentially prohibitive computational requirements. Results are presented for trim, frequency response, poles, and response to pilot inputs, including selected correlations with actual flight test data. The results indicate that when an unsteady airfoil aerodynamic model is used, minor changes occur in the trim pitch settings of the main and tail rotor, the frequency response, and the free-flight response to pilot inputs. These changes slightly improve the correlation with flight test data, and can usually be explained by specific changes in lift distribution over the rotor disk. Noticeable changes can be seen in the poles associated with rotor modes. The effect is typically that of decreasing the damping, although no mode becomes unstable or dangerously lightly damped. Neglecting the effects of the unsteady aerodynamic poles tends to be unconservative.

Nomenclature

C_l, C_d, C_m	=	airfoil section lift, drag, and pitching moments
p, q, r	=	aircraft roll, pitch, and yaw rates
$\boldsymbol{q}$	=	blade modal coefficient vector
t	=	time, s
u, v, w	=	aircraft velocity along body axes
$\boldsymbol{u}$, $\boldsymbol{y}$	=	control and state vectors
$\boldsymbol{x}$	=	unsteady aerodynamics state vector
α	=	blade section angle of attack, rad, or finite state wake coefficient
α_F, β_F	=	angle of attack and sideslip angle of the fuselage
β	=	finite state wake coefficient
θ_0, θ_{1c}, θ_{1s}, θ_{0t}	=	collective, lateral, longitudinal cyclic pitch and tail rotor collective, rad
ϕ_F, θ_F, ψ_F	=	aircraft roll, pitch, and yaw attitude Euler angles, rad

Introduction

SUBSTANTIAL progress has been made recently in the modeling of unsteady aerodynamic effects on the characteristics of helicopter rotor airfoils. Models that are both accurate and relatively simple to implement have become available, and have been incorporated in many helicopter analyses. Most applications have concerned the calculation of rotor vibratory loads and aeroelastic stability, for which unsteady aerodynamic phenomena play a significant role. With the partial exception of Ref. 1, however, little or no information is available on the effects on flight dynamics. Unsteady aerodynamics changes magnitude and phase of the airfoil forces and moments, and consequently, of the lift distribution over the rotor disk. In turn, these changes modify the flapping response, the tip path plane motion, and ultimately the pitching and rolling moments generated by the rotor. For example, unsteady aerodynamics might play a role in the prediction of the off-axis response to cyclic pitch inputs (e.g., the roll response caused by a longitudinal cyclic pitch input). Reference 2 reports the results of a wind-tunnel test in which the off-axis response would have been predicted correctly if a delay in the aerodynamic loads, equivalent to 17 deg of blade azimuth, could have been accounted for. Such delays have been the focus of several recent studies. Arnold et al.[3] have attempted to predict them, using dynamic wake models that are simple extensions of momentum theory. The model accounts for only a portion of the delay required to reproduce off-axis responses from flight test data. The more sophisticated analysis of Rosen and Isser,[4] based on a free-wake model in hover, captures some, but not all, of the cross-coupling effects. Still, both analyses improve considerably the correlation with flight test data, by including the effects of wake dynamics on the motion of the tip path plane. Some additional physical mechanism may yet have to be considered to predict the correct values of the time constants of the aerodynamic loading. Takahashi et al.[5] obtained improved correlation for the off-axis response by introducing a phase delay, calculated from flight test data using system identification techniques, and equal to 36 deg. Modeling of unsteady airfoil aerodynamics can result in phase delays of up to 22–23 deg in airfoil lift, when compressibility is accounted for,[6] and might be important for accurate predictions.

Unsteady airfoil aerodynamic models are available in both state-space and time-marching form. Including either form in a time-marching, free-flight response analysis is rather straightforward. State-space formulations are preferable for stability and frequency response calculations because all of the states of the problem are available explicitly. These formulations can be easily included in stability analyses, although the total number of states may become large. A much greater computational challenge is the calculation of the trim state of the helicopter, including the steady motion of the rotor blades. If one uses methods based on harmonic balance or the Galerkin method,[7] then each unsteady aerodynamic state must be expanded in a truncated Fourier series. The coefficients of the expansion become unknowns of the trim problem. Because there are several coefficients for each state, the size of the trim problem grows rapidly, and the solution cost can become prohibitive. A detailed description of trim methodologies is beyond the scope of this paper; a thorough review has been recently presented by Peters and Barwey.[8] One popular technique is periodic

Received April 10, 1996; revision received Dec. 11, 1996; accepted for publication Dec. 11, 1996.

*Graduate Research Assistant, Center for Rotorcraft Education and Research, Department of Aerospace Engineering. Student Member AIAA.

†Associate Professor, Center for Rotorcraft Education and Research, Department of Aerospace Engineering. Member AIAA.

shooting,[9] which consists of solving the equations of motion over one rotor period, and iterating on controls and initial conditions until a periodic solution is achieved. When unsteady aerodynamics is included, this technique too becomes computationally very expensive. A recent study[10] indicates that a solution with 136 states may require as much as 8.5×10^5 s of CPU time. A massively parallel implementation can reduce this time to about 10^3 s. The alternative is to switch to a time-marching unsteady aerodynamic model for trim, and to neglect unsteady aerodynamic effects on stability and frequency response.

Based on this brief literature review, this paper has the following objectives:

1) To discuss the incorporation of an unsteady aerodynamic model in a nonreal-time, blade-element-type flight dynamic simulation. The mathematical model includes rigid body dynamics and the coupled flap–lag–torsional dynamics of flexible rotor blades. The unsteady aerodynamic model is in state-space form.

2) To present a new method for the calculation of the trim state of the helicopter when a state-space unsteady aerodynamic model is included. This method is based on a Galerkin technique, suitably modified to exploit the mathematical structure of the aerodynamic model.

3) To describe some effects of unsteady aerodynamics on trim, frequency response, coupled rotor/fuselage stability, and free-flight response to pilot inputs, for an articulated rotor helicopter. Comparisons with flight test data are also presented.

Mathematical Model

Overview

The basic mathematical model of the helicopter is described in detail in Ref. 11. A brief overview will be provided in this section.

The mathematical model is formulated in state-space form. That is, the nonlinear equations of motion of the aircraft are expressed as

$$\dot{\boldsymbol{y}} = \boldsymbol{f}(\boldsymbol{y}, \boldsymbol{u}, t) \tag{1}$$

The state vector is defined as

$$\boldsymbol{y} = [\boldsymbol{y}_{\mathrm{RB}}^T \boldsymbol{y}_R^T \boldsymbol{y}_W^T \boldsymbol{y}_U^T \boldsymbol{y}_O^T]^T \tag{2}$$

The vector $\boldsymbol{y}_{\mathrm{RB}}$ is composed of the rigid body linear and angular velocities and of the Euler angles describing the aircraft attitude:

$$\boldsymbol{y}_{\mathrm{RB}}^T = [u\ v\ w\ p\ q\ r\ \phi_F\ \theta_F\ \psi_F] \tag{3}$$

The vector $\boldsymbol{y}_R$ in Eq. (2) contains the rotor states. The blade model is based on a Bernoulli–Euler beam theory suitable for moderately large elastic blade deflections in flap, lag, and torsion. The resulting partial differential equations of motion are transformed into a system of ordinary differential equations using a Galerkin finite element method. A modal coordinate transformation is then performed to reduce the number of rotor degrees of freedom. The dynamics of each blade is modeled independently. Therefore, if the rotor has N_b blades, and M modal coordinates are used to represent the dynamics of each blade, there will be a total of $2N_bM$ states. The equations of motion of the blade are formulated in a rotating coordinate system, and a multiblade coordinate transformation is performed to transform the states to the body-fixed coordinate system. Thus, $\boldsymbol{y}_R$ has the form

$$\boldsymbol{y}_R^T = [q_0^1\ q_{1c}^1\ q_{1s}^1\ q_2^1 \cdots q_0^j\ q_{1c}^j\ q_{1s}^j\ q_2^j \cdots q_0^M\ q_{1c}^M\ q_{1s}^M\ q_2^M] \tag{4}$$

where the superscript j refers to the jth mode. All of the results of this paper refer to a four-bladed rotor and have been obtained using five modes for each blade, for a total of 40 states. The vector $\boldsymbol{y}_W$ in Eq. (2) contains the states that describe the inflow dynamics. The Peters and Cheng[12] finite state wake model is used. The number of states depends on the number of azimuthwise harmonics and radial-shape functions used to describe the inflow distribution. For all of the results of this paper, two harmonics and second-order polynomial shape functions are used, for a total of six states. In the notation of Ref. 12, the vector $\boldsymbol{y}_W$ is given by

$$\boldsymbol{y}_W^T = [\alpha_1^0\ \alpha_2^0\ \alpha_1^1\ \alpha_2^1\ \beta_1^1\ \beta_2^1] \tag{5}$$

The vector $\boldsymbol{y}_U$ in Eq. (2) contains the unsteady aerodynamic states. The presence of this vector, and of the corresponding governing equations, is the main difference between the model of Ref. 11 and that of the present study. The number of elements in $\boldsymbol{y}_U$ depends on the number of blades and spanwise stations at which the unsteady aerodynamic coefficients are calculated. For all of the results presented in this paper, five stations per blade were used, giving a total size of 160 states for the $\boldsymbol{y}_U$. Finally, $\boldsymbol{y}_O$ in Eq. (2) contains three additional states. One is used to describe the tail rotor dynamic inflow; the other two model the delay of the downwash and sidewash on the tail surfaces.[13] For the results of this paper, the state vector therefore has a total of 218 components.

The vector $\boldsymbol{u}$ contains the values of the pitch controls

$$\boldsymbol{u}^T = [\theta_0\ \theta_{1s}\ \theta_{1c}\ \theta_t] \tag{6}$$

Unsteady Aerodynamic Model

The unsteady aerodynamics model used in the present study is the state-space version of the Leishman–Beddoes attached flow model. The model is described in detail in Ref. 6, therefore, only the aspects related to its implementation in the present study will be discussed. The unsteady normal force and pitching moment coefficients of the airfoil C_n and C_m are described at a given spanwise location by eight state equations. In matrix form, the equation for a single spanwise location is

$$\dot{\boldsymbol{x}} = A\boldsymbol{x} + B\boldsymbol{u} \tag{7}$$

$$\begin{Bmatrix} C_n \\ C_m \end{Bmatrix} = C\boldsymbol{x} + D\boldsymbol{u} \tag{8}$$

where A is a diagonal matrix, $\boldsymbol{u} = [\alpha\ q]^T$, and all of the matrices have constant coefficients. Equations (7) and (8) have to be written once for each of R radial stations and each of N_b blades. The quantity $B\boldsymbol{u}$ is a function of the airfoil angle-of-attack α and pitch rate q only. The elements of A are based on the local airspeed, chord length, Mach number, and a number of constants based on both theoretical results and empirical comparisons. Once C_n and C_m are known, the C_l and C_d for the airfoil are given by[6]

$$C_d = C_{d_0} + (1 - \eta)C_n \sin\alpha - C_c \cos\alpha \tag{9}$$

$$C_l = \frac{C_n - C_d \sin\alpha}{\cos\alpha} \tag{10}$$

where C_{d_0} is the component of the profile drag caused by friction, η is a pressure recovery coefficient, and C_c is the chord force coefficient, associated with the pressure drag arising from circulatory loading on the aerofoil.[6] If we denote by $\boldsymbol{x}^{jr}$ the vector of aerodynamic states at the jth spanwise location of the rth blade, then the vector $\boldsymbol{y}_U$ in Eq. (2) is defined as

$$\boldsymbol{y}_U^T = [(\boldsymbol{x}^{11})^T (\boldsymbol{x}^{21})^T \cdots (\boldsymbol{x}^{R1})^T \cdots (\boldsymbol{x}^{1N_b})^T (\boldsymbol{x}^{2N_b})^T \cdots (\boldsymbol{x}^{RN_b})^T] \tag{11}$$

It should be noted that this two-dimensional unsteady aerodynamics model is used in this study simultaneously with the

finite state wake model. Therefore, it has been implicitly assumed that these two analyses model independent unsteady aerodynamic phenomena. This assumption is probably reasonable if only one or two wake harmonics are retained, but will rapidly break down as the number of harmonics is increased. Four harmonics can predict with sufficient accuracy shed wake effects,[12] and in that case the effects of the shed wake would be counted twice, once by the unsteady airfoil model and once by the wake model.

Solution Method

Calculation of Trim State

The trim algorithm used in this study has an inner-loop/outer-loop structure. The vector $\boldsymbol{x}_c$ of trim unknowns is partitioned into a vector $\boldsymbol{x}_{\mathrm{OL}}$ of primary, or outer-loop unknowns and a vector $\boldsymbol{x}_{\mathrm{IL}}$ of secondary, or inner-loop unknowns. The former includes all of the trim variables of the problem, except for those associated with unsteady aerodynamics, which are instead included as inner-loop unknowns. Thus,

$$\boldsymbol{x}_c = \begin{Bmatrix} \boldsymbol{x}_{\mathrm{OL}} \\ \boldsymbol{x}_{\mathrm{IL}} \end{Bmatrix} \tag{12}$$

Outer Loop

The outer-loop procedure is very similar to the general trim procedure used in Ref. 7, therefore, only a brief outline will be provided here. The vector $\boldsymbol{x}_{\mathrm{OL}}$ of trim variables is composed of a vector $\boldsymbol{x}_R$ of rotor trim variables, a vector $\boldsymbol{x}_A$ of aircraft trim variables, and a vector $\boldsymbol{x}_O$ of wake and downwash delay trim variables, that is,

$$\boldsymbol{x}_{\mathrm{OL}} = \begin{Bmatrix} \boldsymbol{x}_R \\ \boldsymbol{x}_A \\ \boldsymbol{x}_O \end{Bmatrix} \tag{13}$$

The calculation of the rotor portion of the trim is based on the assumption that the blades are identical and perform identical motions in trimmed flight. Therefore, it is only necessary to consider the motion of a reference blade. The motion of the blade is described by a vector $\boldsymbol{q}(\psi)$ of generalized coordinates, which are the time-varying coefficients of the modal expansion before the application of the multiblade coordinate transformation. The vector $\boldsymbol{q}(\psi)$ is approximated by a truncated Fourier series:

$$\boldsymbol{q}(\psi) \approx \boldsymbol{q}_{\mathrm{app}}(\psi) = \boldsymbol{q}_0 + \sum_{k=1}^{H} (\boldsymbol{q}_{kc} \cos k\psi + \boldsymbol{q}_{ks} \sin k\psi) \tag{14}$$

where $\boldsymbol{q}_0$, $\boldsymbol{q}_{kc}$, and $\boldsymbol{q}_{ks}$ are constant vectors of size M, if M modes have been retained in the modal coordinate transformation. Therefore, the vector $\boldsymbol{x}_R$ in Eq. (13) is given by

$$\boldsymbol{x}_R = [\boldsymbol{q}_0^T \; \boldsymbol{q}_{1c}^T \; \boldsymbol{q}_{2c}^T \cdots \boldsymbol{q}_{Hc}^T \; \boldsymbol{q}_{1s}^T \; \boldsymbol{q}_{2s}^T \cdots \boldsymbol{q}_{Hs}^T]^T \tag{15}$$

and has size $M(2H + 1)$. The vector $\boldsymbol{x}_A$ of aircraft trim unknowns in Eq. (13) is given by

$$\boldsymbol{x}_A = [p \; q \; r \; \phi_F \; \theta_F \; \alpha_F \; \beta_F \; \theta_0 \; \theta_{1s} \; \theta_{1c} \; \theta_t]^T \tag{16}$$

in which all of the quantities are to be taken as constant trim values. Finally, the subvector $\boldsymbol{x}_O$ of trim unknowns is composed of eight elements. The first six are identical to those in the vector $\boldsymbol{y}_W$ in Eq. (5), except that here they are to be seen as constant trim values. The remaining two are the trim values of the downwash delay over the tail surfaces.[14] Therefore, the total number of elements in $\boldsymbol{x}_{\mathrm{OL}}$ is $M(2H + 1) + 19$.

In general, a trial trim solution corresponding to $\boldsymbol{x}_{\mathrm{OL}}$ will not satisfy the equations of motion of the reference blade. This means that if the equations are written with all of the terms on the left-hand side of the equal sign, the quantity on the right-hand side (RHS) will typically not be zero, but a time-dependent residual vector $\boldsymbol{r}(\psi)$. Based on Galerkin's method, the best choice of $\boldsymbol{x}_{\mathrm{OL}}$ is that which satisfies the following conditions:

$$\int_0^{2\pi} \boldsymbol{r}(\psi)\, \mathrm{d}\psi = 0$$

$$\int_0^{2\pi} \boldsymbol{r}(\psi) \cos k\psi \, \mathrm{d}\psi = 0 \qquad k = 1, \ldots, H \tag{17}$$

$$\int_0^{2\pi} \boldsymbol{r}(\psi) \sin k\psi \, \mathrm{d}\psi = 0 \qquad k = 1, \ldots, H$$

Because $\boldsymbol{r}(\psi)$ has size M, Eq. (17) is a system of $M(2H + 1)$ nonlinear algebraic equations; the unknowns are the elements of $\boldsymbol{x}_{\mathrm{OL}}$. Another 11 algebraic equations in the same unknowns can be obtained by writing six equations enforcing overall force and moment equilibrium on the aircraft; three equations enforcing the kinematic relations between the trim values of pitch, roll, and yaw rates and the trim values of the time derivatives of the Euler angles of the aircraft; one equation enforcing turn coordination; and one equation consisting of a kinematic condition that involves the flight-path angle.[7,15] Finally, eight equations can be obtained by requiring that all of the wake and downwash states have a constant average value. Therefore, $M(2H + 1) + 19$ algebraic equations are available to determine an identical number of trim unknowns. In this portion of the trim solution, the trim values associated with the unsteady aerodynamic states are assumed to be known, and are held fixed.

Inner Loop

The objective of the inner-loop procedure is to determine the portion $\boldsymbol{x}_{\mathrm{IL}}$ of the trim vector. The unsteady aerodynamic coefficients are defined in the rotating coordinate system and will typically have a periodic variation in trimmed flight. As in the outer loop, only the trim state of a reference blade needs to be considered. The inner-loop procedure is also based on Galerkin's method. Therefore, the starting point is the approximation of the vector of aerodynamic states $\boldsymbol{x}^r(\psi)$ at the rth spanwise station with a truncated Fourier series

$$\boldsymbol{x}^r(\psi) \approx \boldsymbol{x}^r_{\mathrm{app}}(\psi) = \boldsymbol{x}_{r0} + \sum_{k=1}^{H} (\boldsymbol{x}_{rkc} \cos k\psi + \boldsymbol{x}_{rks} \sin k\psi) \tag{18}$$

where $\boldsymbol{x}_{r0}$, $\boldsymbol{x}_{rkc}$, and $\boldsymbol{x}_{rks}$ are constant vectors of size 8. Equation (18) must be written once for each of the R spanwise stations at which the unsteady aerodynamic coefficients are calculated. Therefore, the vector $\boldsymbol{x}_{\mathrm{IL}}$ of unsteady aerodynamic trim unknowns is given by

$$\boldsymbol{x}_{\mathrm{IL}} = [\boldsymbol{x}_{1U}^T \; \boldsymbol{x}_{2U}^T \cdots \boldsymbol{x}_{RU}^T]^T \tag{19}$$

where the generic subvector $\boldsymbol{x}_{rU}$ contains the coefficients of the harmonics in Eq. (18) at the rth spanwise station, is defined as

$$\boldsymbol{x}_{rU} = [\boldsymbol{x}_{r0}^T \; \boldsymbol{x}_{r1c}^T \; \boldsymbol{x}_{r2c}^T \cdots \boldsymbol{x}_{rHc}^T \; \boldsymbol{x}_{r1s}^T \; \boldsymbol{x}_{r2s}^T \cdots \boldsymbol{x}_{rHs}^T]^T \tag{20}$$

and has size $8(2H + 1)$. Therefore, the vector $\boldsymbol{x}_{\mathrm{IL}}$ contains a total of $8R(2H + 1)$ unknowns.

The truncated Taylor-series expansion, Eq. (18), is then substituted into the unsteady aerodynamic equations, Eq. (7). In general, the equations will not be identically satisfied, and there will be a nonzero, time-dependent residual vector $\boldsymbol{r}^r_U(\psi)$ given by

$$\boldsymbol{r}^r_U(\psi) = \dot{\boldsymbol{x}}^r_{\mathrm{app}} - A\boldsymbol{x}^r_{\mathrm{app}} - B\boldsymbol{u}^r \tag{21}$$

where the vector $\boldsymbol{u}^r$ contains the angle of attack and pitch rate of the rth spanwise cross section, calculated from the outer-loop solution $\boldsymbol{x}_{OL}$, which is held fixed in the inner-loop solution. The matrices A and B are also calculated based on $\boldsymbol{x}_{OL}$. According to the Galerkin method, the choice of $\boldsymbol{x}_{r0}$, $\boldsymbol{x}_{rks}$, and $\boldsymbol{x}_{rkc}$, that minimizes the residual $\boldsymbol{r}_U^r(\psi)$, is that which satisfies

$$\int_0^{2\pi} \boldsymbol{r}_U^r(\psi)\, d\psi = 0$$

$$\int_0^{2\pi} \boldsymbol{r}_U^r(\psi)\cos k\psi\, d\psi = 0 \qquad k = 1, \ldots, H \tag{22}$$

$$\int_0^{2\pi} \boldsymbol{r}_U^r(\psi)\sin k\psi\, d\psi = 0 \qquad k = 1, \ldots, H$$

These equations make up a system of $2H + 1$ vector equations or $8(2H + 1)$ scalar equations, that has to be written at each of R spanwise station. This yields a total of $8R(2H + 1)$ scalar equations, that are solved for the $8R(2H + 1)$ elements of the unsteady aerodynamic trim vector $\boldsymbol{x}_{IL}$. For fixed $\boldsymbol{x}_{OL}$, the solution at one spanwise station is decoupled from those at the remaining stations. Therefore, it is not necessary to form a system of $8R(2H + 1)$ simultaneous equations, because it is possible to solve R separate smaller systems of $8(2H + 1)$ equations, which is far more efficient computationally.

Organization of the Inner-/Outer-Loop Trim Procedure

The flight condition for which the trim solution is sought is defined by the values of advance ratio μ, turn rate ψ_F, and flight-path angle γ. The system of nonlinear algebraic equations that make up the outer-loop problem can be written symbolically in the form $\boldsymbol{f}(\boldsymbol{x}_{OL}) = 0$. If $\boldsymbol{x}_{OL}$ is not the exact solution, the RHS of the system will be equal to a nonzero residual vector $\boldsymbol{r}_O$. Most nonlinear algebraic equation solvers, including that used in the present study,[16] require the value of the residual vector $\boldsymbol{r}_O$ for a given tentative value of $\boldsymbol{x}_{OL}$; the solver then attempts to select the value of $\boldsymbol{x}_{OL}$ that makes $\boldsymbol{r}_O = 0$.

The trim procedure begins with an initial guess for $\boldsymbol{x}_{OL}$. At every iteration of the solution the nonlinear equation solver provides an approximation for $\boldsymbol{x}_{OL}$, corresponding to a given motion of rotor, fuselage, and inflow. For a given iteration, the following steps are performed:

1) With the given value of $\boldsymbol{x}_{OL}$, the quantities A, B, and $\boldsymbol{u}$ in Eq. (7) are calculated. These are functions of blade radial coordinate and azimuth angle, and are held fixed for the rest of the iteration.

2) The values of A, B, and $\boldsymbol{u}$ are used to determine $\boldsymbol{x}_{IL}$. From $\boldsymbol{x}_{IL}$ it is possible to calculate C_l, C_d, and C_m as a function of blade station and azimuth angle using Eqs. (10), (9), and (8), respectively.

3) The distributions of C_l, C_d, and C_m are substituted in the equations of the outer-loop problem, together with the approximation for $\boldsymbol{x}_{OL}$. This yields the value of the residual $\boldsymbol{r}_O$ required by the algebraic equation solver, and concludes the iteration.

The trim procedure terminates when successive approximations for $\boldsymbol{x}_{OL}$ differ by less than a specified tolerance.

Linearization and Free-Flight Response Calculation

The extraction of a linearized model and the calculation of the free-flight response to arbitrary pilot inputs are carried out along the same general lines of Refs. 13 and 14. The linearized model is obtained by perturbing Eq. (1) about a trimmed equilibrium position corresponding to the trim solution $\boldsymbol{x}_C$. The elements of the state and control vectors are perturbed one at a time, and the derivatives are calculated using finite difference approximations, resulting in a state matrix A and a control matrix B. A multiblade coordinate transformation is performed on the rotor portions of A and B. The linearized system is then used to derive the frequency response characteristics for the I/O pairs of interest. The free-flight response is calculated by simply integrating Eq. (1) with the required pilot input. The variable-step, variable-order Adams–Bashforth-type solver DE/STEP is used.[17]

Results

The results presented in this section refer to a configuration similar to a Sikorsky UH-60 helicopter with the flight control system turned off. The blades are modeled by four finite elements, and five mode shapes are retained in the modal coordinate transformation. These numbers were found sufficient to obtain accurate results from the mathematical model of this study.[18] More elements may have to be used for hingeless or bearingless rotor configurations. The five blade modes retained are the rigid body modes in lag and flap, and the first elastic modes in flap bending, lag bending, and torsion. All of the quantities required for the calculation of the aerodynamic load distribution were typically calculated using 32 spanwise stations per blade. The unsteady states were calculated at five spanwise stations per blade; spline interpolation was then used to obtain the values at all of the other stations required. Five stations represented the best compromise between accuracy and computational effort. More stations may have to be included if one is interested, for example, in the calculation of vibratory loads or in the dynamics of higher modes. Finally, the flight conditions correspond to an altitude of 5250 ft in a standard atmosphere together with a C_T/σ of 0.081. These are also the conditions present during the collection of the flight test data used to correlate some of the theoretical results of this study. A selection of illustrative results is presented in this section. Many additional results can be found in Ref. 18.

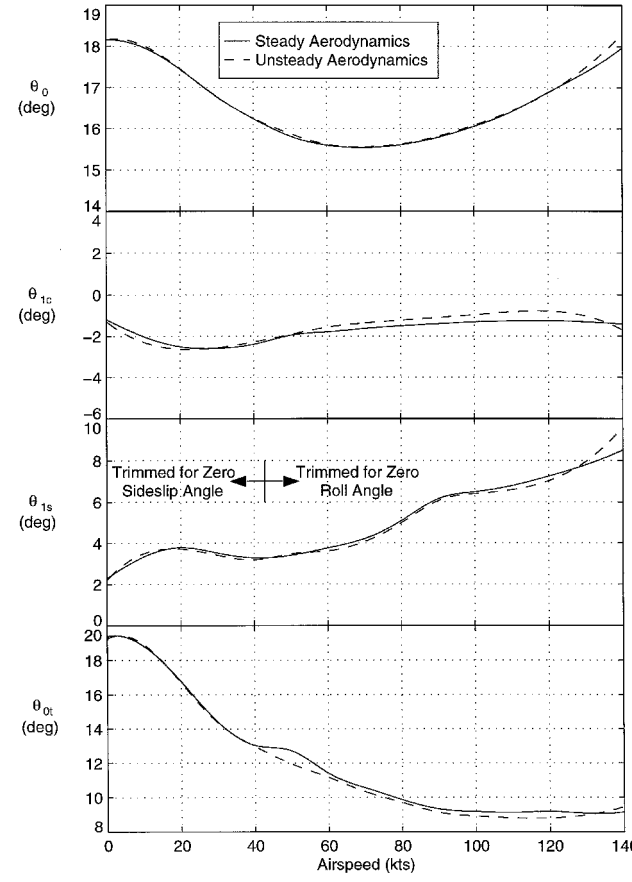

Fig. 1 Comparison of trim swashplate pitch angle variation with airspeed.

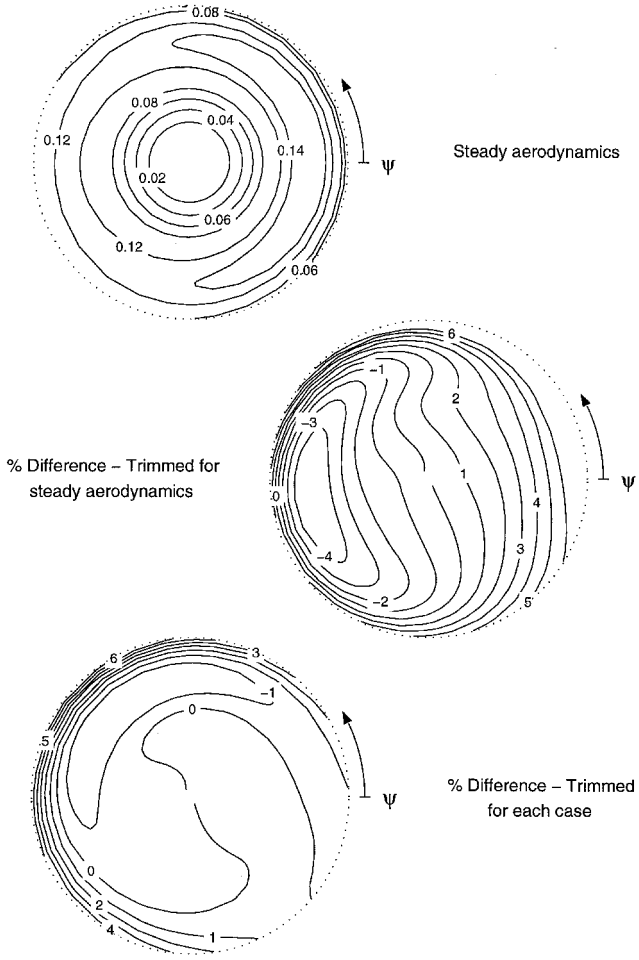

Fig. 2 Contour plots of $C_l M^2$, hover flight condition.

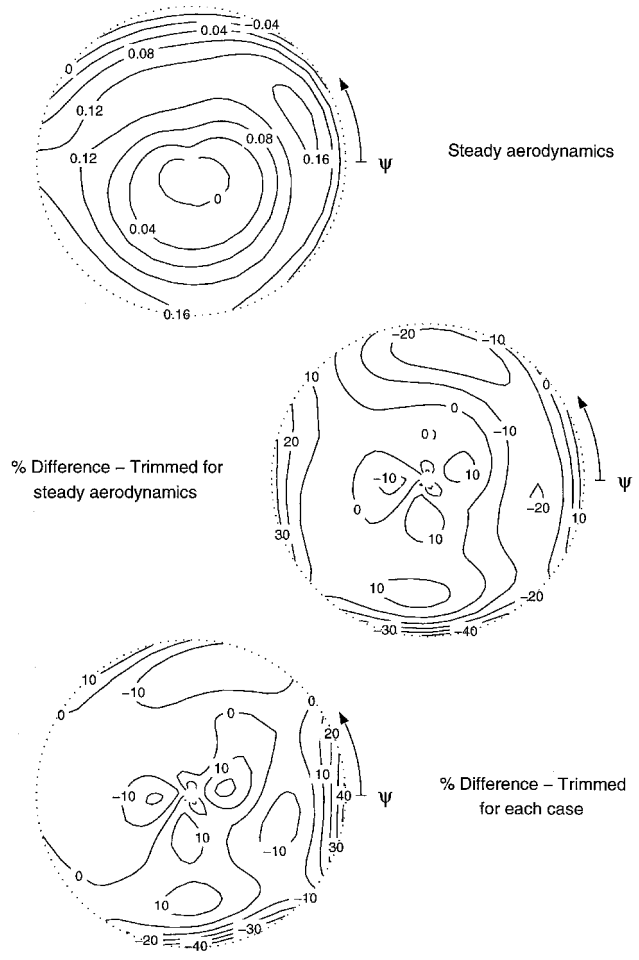

Fig. 3 Contour plots of $C_l M^2$. Forward-flight condition, V = 120 kn.

Trim

Figure 1 compares trim control angles as a function of airspeed calculated using quasisteady and unsteady aerodynamic models. In straight flight there is some ambiguity in the trim solution because lateral force equilibrium can be obtained with combinations of roll angle and sideslip. Therefore, at 50 kn and above, the trim problem is formulated so that the aircraft is trimmed for zero roll angle, whereas the aircraft is trimmed for zero sideslip at lower airspeeds. The figure shows that there is negligible change in the main and tail rotor collective pitch, and a slightly larger difference for the cyclic pitch.

To better understand the effects of unsteady aerodynamics on trim, the lift distributions over the disk have been plotted in Figs. 2 and 3 for the cases of hover and 120 kn, corresponding to about $\mu = 0.28$. The plots show contours of $C_l M^2$, which are representative of the local lift. Each of the figures contains three plots. The top plot shows the distribution of $C_l M^2$ over the rotor disk in trimmed conditions, when a quasisteady aerodynamic model is used. The middle plot is obtained using the unsteady aerodynamic model, but with the controls (and all of the other trim variables) corresponding to the trim with the quasisteady aerodynamics. Therefore, the middle plot generally refers to an untrimmed condition. It should be kept in mind that unsteady aerodynamics has both a direct and an indirect effect on the aerodynamic load distribution. The former is given by the effects on the aerodynamic coefficients. The latter is because of the changes in the pitch settings required to establish trim with the new aerodynamic coefficients, that also translate into changes in angle of attack and pitch rate for each blade section. Thus, the middle plot is indicative of the direct effect of unsteady aerodynamics. Finally, the bottom plot of each figure shows the relative difference between the distributions of $C_l M^2$ at trim calculated using the quasisteady and the unsteady aerodynamic model. Thus, the bottom plot captures the overall effects of unsteady aerodynamics.

The top plot of Fig. 2 shows that the lift distribution in hover is almost axisymmetric; the slight distortions are primarily a result of the cyclic pitch required to maintain side force and roll moment equilibrium in the presence of the tail rotor. Keeping the controls fixed and using the unsteady aerodynamic model results in small changes of lift distribution, which would have been completely absent if the cyclic had been exactly zero. These changes correspond to a slight lift increase toward the tail of the aircraft, and a slight decrease toward the nose. This longitudinal asymmetry induces a small tilt of the tip path plane to the left, when seen from behind, that is compensated with a slightly lower value of lateral cyclic, as shown in Fig. 1. The bottom plot of Fig. 2 shows that the differences between the lift distributions predicted using the two aerodynamic models are small when compared at trim for both cases.

A different pattern appears at V = 120 kn, as shown in Fig. 3. The middle plot of the figure shows that when the controls are kept fixed at the values for the quasisteady aerodynamics case, and unsteady aerodynamics is used, the lift tends to increase on the front end of the disk and decrease on the back end. The changes become significant toward the outer portions of the disk. The resulting changes in aerodynamic flapping moment tend to make the tip path plane tilt to the right, and thus require more lateral cyclic, as shown in Fig. 1.

Frequency Response

For the frequency response curves, comparisons are made between flight test data, numerical results with a quasisteady

aerodynamics formulation,[11] and numerical results with unsteady aerodynamics. The quasisteady aerodynamic model of Ref. 11 determines aerodynamic coefficients based on the instantaneous values of angle of attack and Mach number, using look-up tables that include the effects of stall on the coefficients. The results obtained using unsteady aerodynamic analysis, on the other hand, do not include any stall effects.

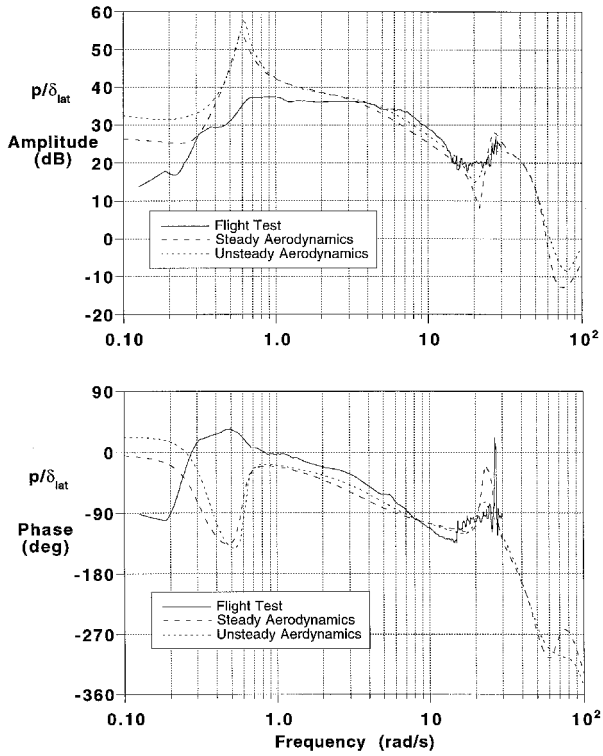

Fig. 4 Effect of unsteady aerodynamics on bare airframe roll-rate frequency response to lateral cyclic input δ_{lat} in hover.

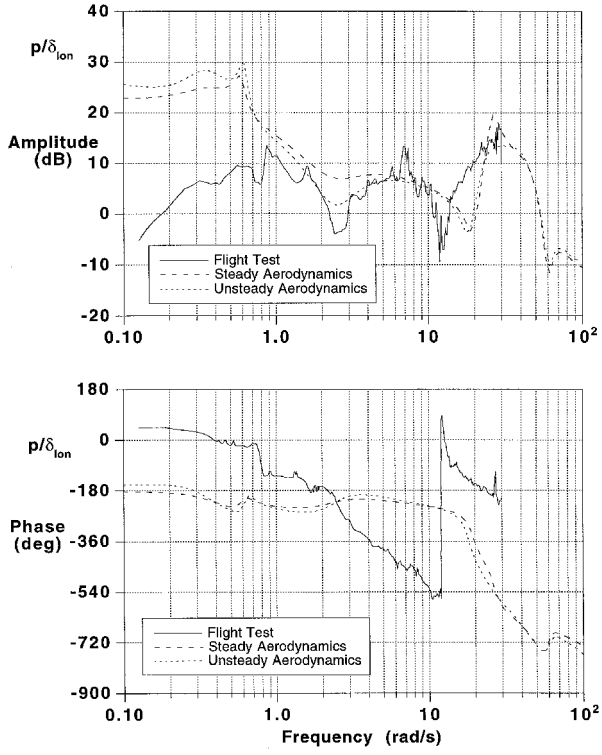

Fig. 5 Effect of unsteady aerodynamics on bare airframe roll-rate frequency response to longitudinal cyclic input δ_{lon} in hover.

Figure 4 shows the roll-rate frequency response caused by a lateral cyclic input in hover. The plot indicates that the addition of unsteady aerodynamics slightly improves the magnitude correlation between about 2–20 rad/s and the phase correlation between about 1–20 rad/s. Coherence estimates indicate that the experimental data are rather unreliable at the high and low ends of the frequency range, and so it is impos-

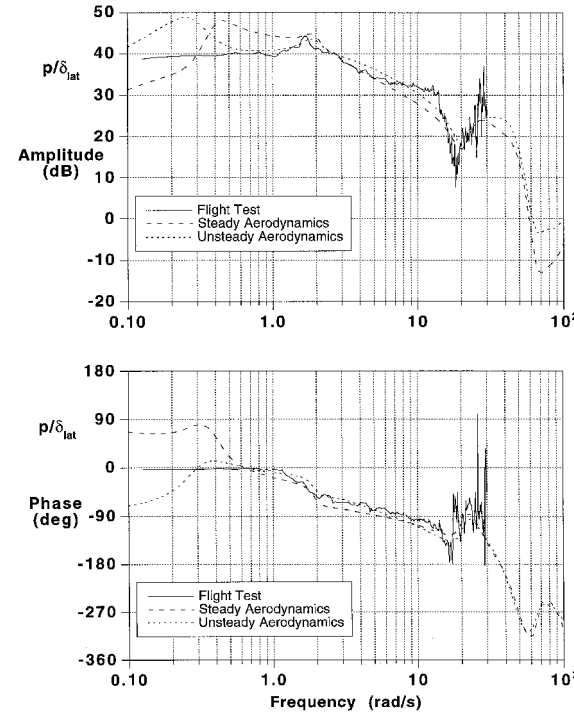

Fig. 6 Effect of unsteady aerodynamics on bare airframe roll-rate frequency response to lateral cyclic input δ_{lat} for 120-kn forward flight.

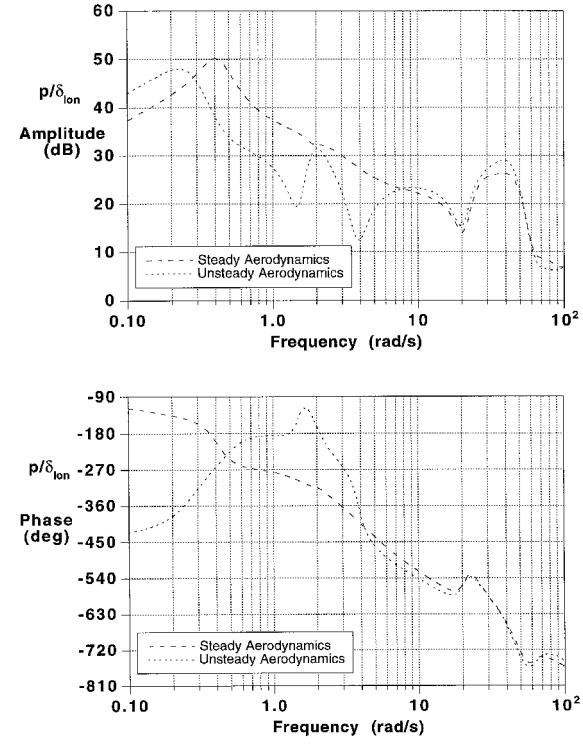

Fig. 7 Effect of unsteady aerodynamics on bare airframe roll-rate frequency response to longitudinal cyclic input δ_{lon} for 120-kn forward flight.

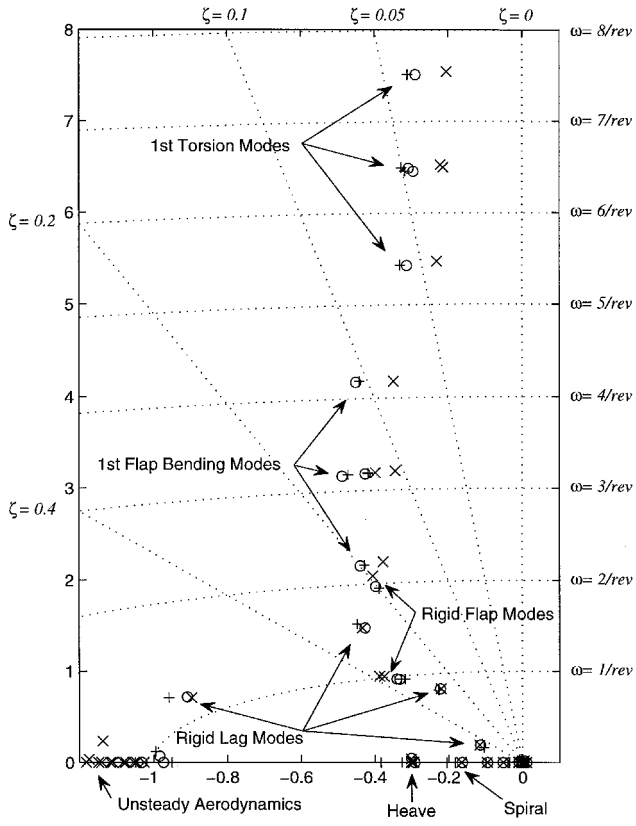

Fig. 8 Effect of unsteady aerodynamics on bare airframe pole locations in hover. +, steady aerodynamics; ○, reduced-order unsteady aerodynamics; and ×, unsteady aerodynamics.

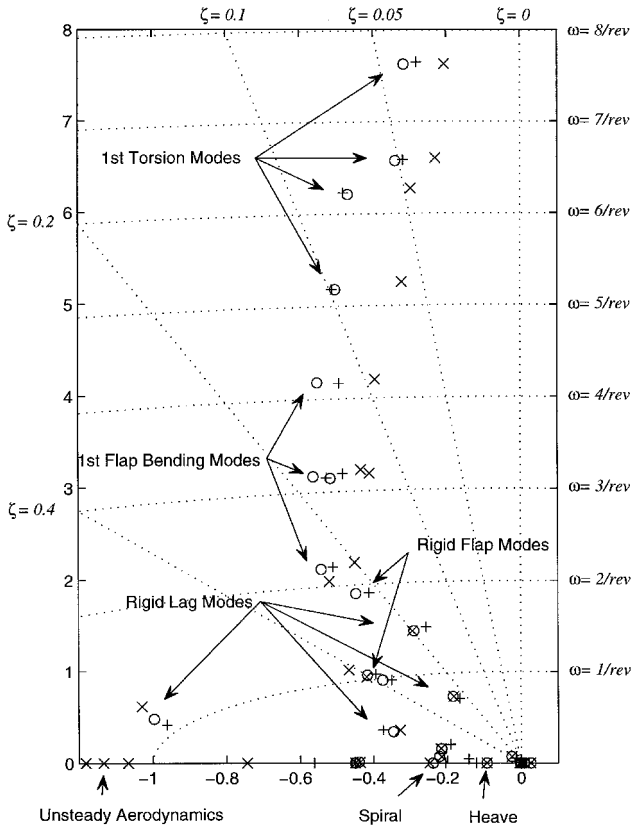

Fig. 9 Effect of unsteady aerodynamics on bare airframe pole locations for 120-kn forward flight. +, steady aerodynamics; ○, reduced-order unsteady aerodynamics; and ×, unsteady aerodynamics.

sible to determine conclusively whether unsteady aerodynamics has improved the correlation at these frequencies. The notch in the magnitude at a frequency around 20 rad/s is associated with the regressive lag mode. Unsteady aerodynamics reduces the overprediction of the frequency of this mode.

Figure 5 shows the frequency response of roll caused by longitudinal cyclic input in hover. Including unsteady aerodynamics improves noticeably the magnitude correlation over the frequency range of about 1 rad/s through 6–7 rad/s. On the other hand, the effect on the phase is minimal, and a substantial discrepancy with the experimental results remains. As mentioned in the Introduction, recent improvements in inflow modeling[3–5] have reduced the error in amplitude and phase predictions for the off-axis response. These improvements have not been included in the present study. Therefore, it is likely that a better inflow model can further improve the correlation in Fig. 5.

Figure 6 shows the on-axis frequency response of the helicopter to lateral cyclic input at 120 kn. The differences between the predictions with quasisteady and unsteady aerodynamics remain fairly small, even at this higher speed, especially for frequencies greater than 1 rad/s. Little or no improvement appears in the correlation with the magnitude test data, whereas a small improvement can be seen in the phase correlation between 1 and 6–7 rad/s. Figure 7 shows the off-axis roll rate response to longitudinal cyclic input for the same 120-kn condition. Flight test results were not available for this flight condition. The differences between results with quasisteady and unsteady aerodynamics are rather significant. The results indicate that using unsteady aerodynamics reveals some dominant poles, particularly for the case of roll caused by longitudinal cyclic. One such pole at around 1.2 rad/s causes a

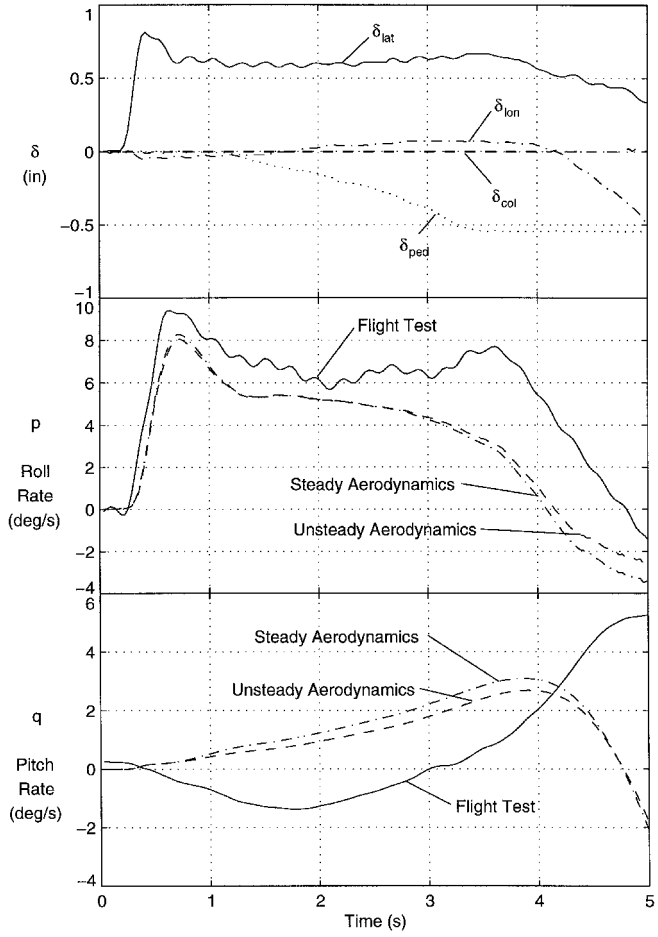

Fig. 10 Response time history comparisons for lateral cyclic step input δ_{lat}. Hover flight condition.

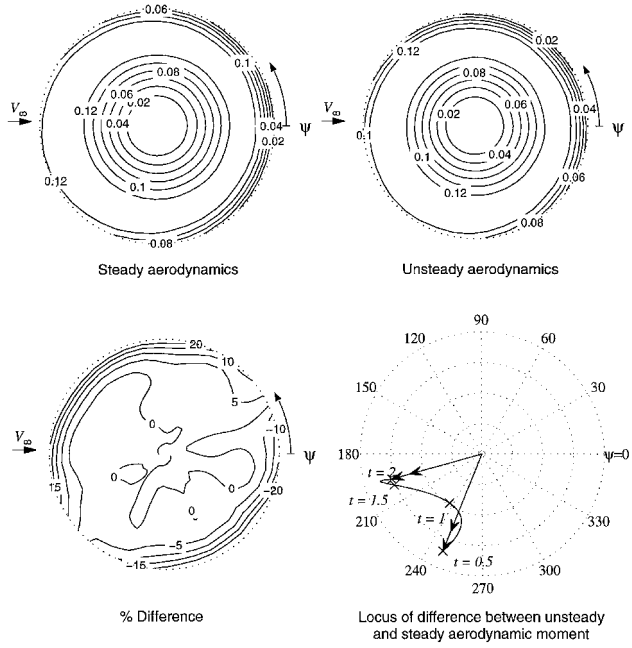

Fig. 11 Contour plots of $C_l M^2$ at $t = 1$ s of response to control perturbation. Hover flight condition.

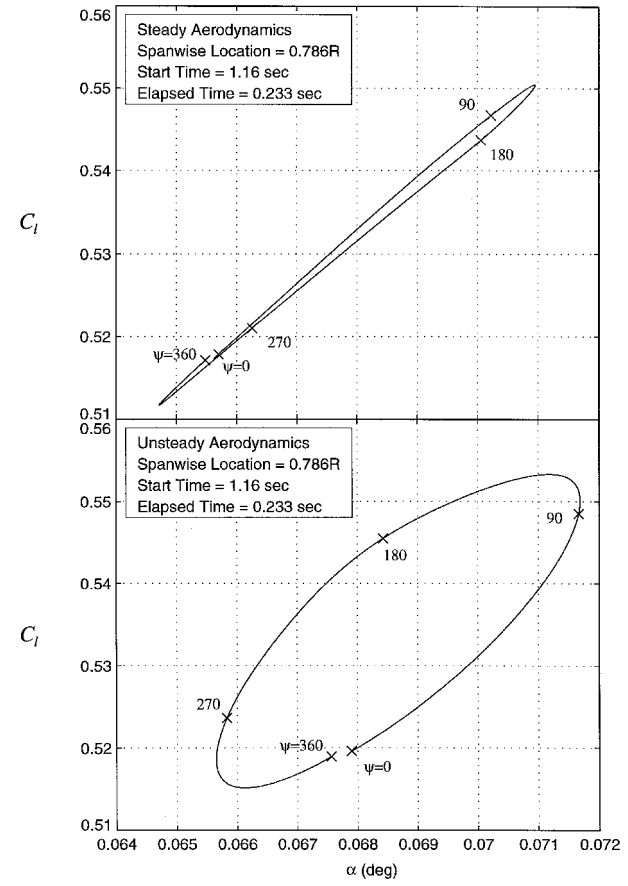

Fig. 12 Comparison of C_l variation with angle of attack during lateral cyclic perturbation in hover.

180-deg phase shift in the response. Because of the absence of flight test data it is not possible to determine whether unsteady aerodynamics improves the correlation.

Figures 8 and 9 show the poles in hover and at a speed of 120 kn, respectively. Each figure shows three types of poles. The first two are obtained using a quasisteady aerodynamic model and the unsteady aerodynamic model, respectively. The third type, denoted in the figures by reduced order unsteady aerodynamics, is obtained by condensing out the unsteady aerodynamic states. This is done by partitioning the state vector $\boldsymbol{y}$ of Eq. (2) into a subvector $\boldsymbol{y}_U$ of unsteady aerodynamic states to be condensed out, and another subvector $\boldsymbol{y}_O$ containing all
of the other states. The state matrix A is partitioned accordingly, that is,

$$\begin{Bmatrix} \dot{\boldsymbol{y}}_O \\ \dot{\boldsymbol{y}}_U \end{Bmatrix} = \begin{bmatrix} A_{RR} & A_{RU} \\ A_{UR} & A_{UU} \end{bmatrix} \begin{Bmatrix} \boldsymbol{y}_O \\ \boldsymbol{y}_U \end{Bmatrix} \tag{23}$$

and the assumption is made that $\dot{\boldsymbol{y}}_U = 0$. Obtaining then $\boldsymbol{y}_U$ as a function of $\boldsymbol{y}_O$ yields

$$\dot{\boldsymbol{y}}_O = (A_{RR} - A_{RU}A_{UU}^{-1}A_{UR})\boldsymbol{y}_U = A_{\text{RED}}\boldsymbol{y}_O \tag{24}$$

This condensation is equivalent to assuming that the unsteady aerodynamic poles are infinitely fast. The poles of the reduced matrix A_{RED} are the third type of poles shown in Figs. 8 and 9. The figures also show lines of constant natural frequency, that appear as ellipses because of the scales of the x and y axes, and lines of constant damping ratio.

The principal effect of unsteady aerodynamics for this configuration appears to be on the damping of the main rotor modes. It should be noted that while the modes are identified as torsion, flap, or lag modes, these modes are significantly coupled, especially with the rigid body modes of the entire aircraft. In hover, the unsteady aerodynamic poles appear clustered on the real axis, at frequencies of 1/rev and above. In forward flight at 120 kn (Fig. 9), they tend to remain on the real axis, but spread out and move to higher frequencies. It is apparent from Figs. 8 and 9 that reducing the order of the linearized model by condensing out the unsteady aerodynamic

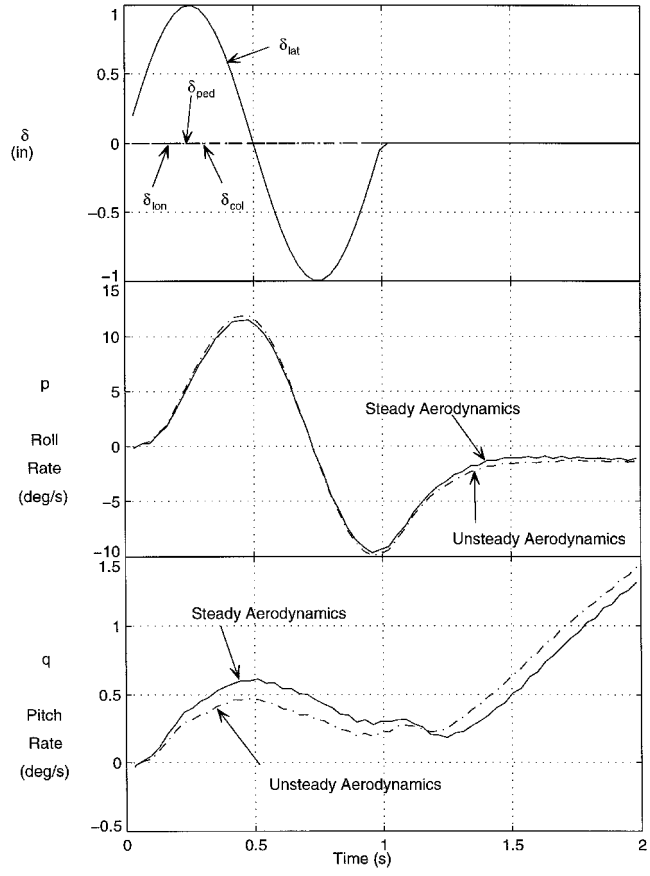

Fig. 13 Response time history comparisons for lateral cyclic doublet input δ_{lat}. Forward-flight condition, $V = 120$ kn.

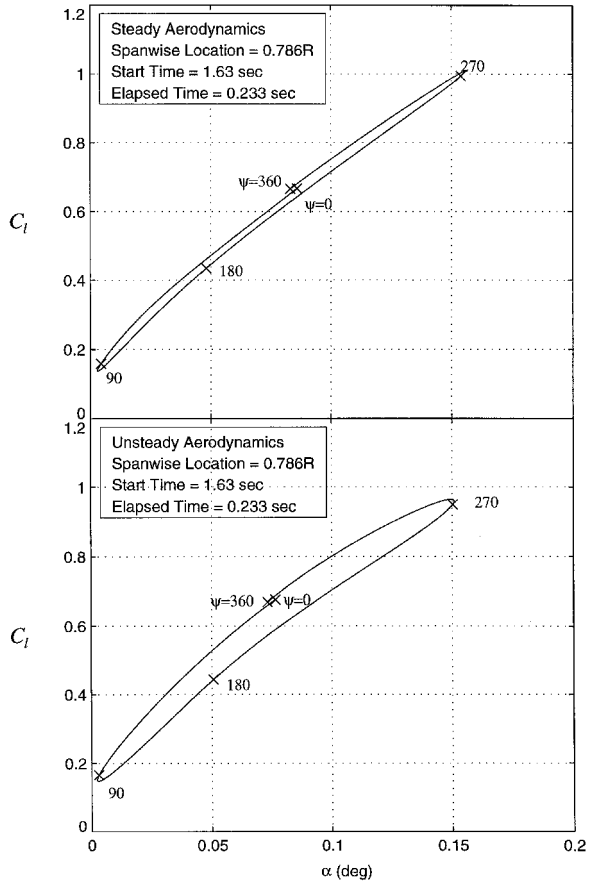

Fig. 14 Comparison of C_l variation with angle of attack during lateral cyclic perturbation at 120-kn forward flight.

states substantially masks their effects. Especially in hover, the condensation produces results that are almost identical to those that would have been obtained if unsteady aerodynamics had not been modeled at all.

Free-Flight Response

The time history plots of Fig. 10 compare the calculated and actual flight test response of the aircraft to a given set of control movements approximating a lateral cyclic step input in hover. The calculated and actual trim settings were not precisely the same. Therefore, to produce the simulated time histories, the time histories of the flight test control inputs were applied as perturbations from the calculated trim control positions. Simulation results were generated using both the quasisteady and unsteady aerodynamics models and are shown in the comparison. These plots show there is a reasonable qualitative agreement for the on-axis response, although the roll rates are somewhat underpredicted. Unsteady aerodynamics marginally improves the correlation. Substantial differences remain in the prediction of the sign of the off-axis response, even if unsteady aerodynamics produces a small improvement.

Figure 11 shows the distribution of $C_l M^2$ over the rotor disk at time $t = 1$ s, corresponding to the control inputs and response shown in Fig. 10. The upper left plot shows the $C_l M^2$ distribution calculated using the quasisteady aerodynamic model, the upper right plot that calculated using the unsteady aerodynamic model, and the lower left plot shows the relative difference between the two. The lower right polar plot illustrates the variation with time of the difference between quasisteady aerodynamic and unsteady aerodynamics total moment acting on the hub. The aerodynamic moment vector being located in the third quadrant therefore indicates that unsteady aerodynamics reduces both the rolling moment and the pitching moment compared with quasisteady aerodynamics. The tip path plane responds with a slightly larger flapping over the nose and to the left, resulting in lower pitch and roll rates.

That unsteady aerodynamics effects are really taking place can be seen from Fig. 12, which shows the variation of C_l with angle of attack for both the quasisteady and unsteady cases throughout one complete rotor revolution during the step response at about 79% span. The typical elliptical shape of the unsteady $C_l(\alpha)$ plot is evident in Fig. 12, but the corresponding changes of C_l with respect to the quasisteady case are quite small.

The response to a doublet-type input of lateral cyclic in forward flight at $V = 120$ kn is shown in Fig. 13. Because flight test data for this flight condition were not available, only calculated results are shown in the figure. The simulated control inputs are measured from the respective trim values. The results indicate that the model with unsteady aerodynamics predicts slightly higher roll rates to the right, when seen from behind, or, correspondingly, lower roll rates to the left. The pitch rate q predicted with the unsteady model is initially lower (less nose up), indicating a slight decrease in the off-axis response. Finally, Fig. 14 shows the $C_l(\alpha)$ relationship for a cross section at approximately 79% span, for a full rotor revolution starting at $t = 1.6$ s from the beginning of the doublet maneuver, obtained using the quasisteady and the unsteady aerodynamic model. In both cases the time variations of α are a result of the trim values of collective and cyclic pitch, to changes in inflow because of wake dynamics and the rigid body motion of the helicopter, and to the elastic motion of the blades. The effect of unsteadiness is clearly much more pronounced at this speed than it was at hover with changes in C_l of 10–15% for given α, for most values of the angle of attack.

Summary and Conclusions

This paper presented a study of the effects of unsteady airfoil aerodynamics on several flight dynamics characteristics of an articulated rotor helicopter. The mathematical model was obtained by coupling the state-space version of the Leishman unsteady aerodynamic model for attached flow to an existing blade-element-type flight dynamic analysis that includes a flexible rotor blade model. A new trim algorithm was developed to deal with the unsteady aerodynamic states in a computationally efficient way. Results were presented for trim, frequency response, poles, and response to pilot inputs. Some of these results were correlated with flight test data. In all cases the rotor was moderately loaded.

The results presented in this paper indicate the following effects of incorporating unsteady airfoil aerodynamics in the model of an articulate rotor aircraft:

1) Very minor changes occur in the trim values of main rotor collective and longitudinal cyclic pitch, and of tail rotor collective. Slightly larger, but still modest, changes occur in the lateral cyclic pitch. These can be explained by the changes in lift distribution over the rotor disk.

2) Some minor differences can be seen in the on-axis frequency response. Both in hover and forward flight, these changes slightly improve the correlation with flight test data. More significant changes occur in the off-axis response, especially in the magnitude of the response. For the case of hover, for which flight test data were available, the changes improve the magnitude correlation between the frequencies of about 1 and 6–8 rad/s. On the other hand, no significant improvement occurs in the phase correlation. The correlation can probably be improved further by incorporating recent results on inflow dynamics in maneuvers, which were not considered in the present study.

3) Noticeable changes can be seen in the poles associated with rotor modes. The effect is typically that of decreasing the damping, although no mode becomes unstable or dangerously lightly damped. Neglecting the effects of the unsteady aerodynamic poles, for example, by condensing them out of the

model, hides this decrease in damping, therefore, it may be unconservative. In this case the poles are essentially the same as those predicted by a model that does not include unsteady aerodynamics at all.

4) Some small differences can be observed in the free-flight response to pilot inputs, especially in forward flight at higher speeds. These differences can be explained by changes in lift distribution over the rotor disk. In hover, for which comparisons with flight test data were presented, some minor improvements in correlation were visible.

Acknowledgments

The authors acknowledge the support for this research work by the Army Research Office under the Center for Rotorcraft Education and Research Contract DAAH-04-94-G-0074. The Technical Monitor was Tom Doligalski. The flight test data were provided by Mark Tischler, U.S. Army, NASA Ames Research Center.

References

[1]He, C.-J., and Du Val, R., "An Unsteady Airload Model with Dynamic Stall for Rotorcraft Simulation," *Proceedings of the 50th Annual Forum of the American Helicopter Society* (Washington, DC), American Helicopter Society, Alexandria, VA, 1994, pp. 931–948.

[2]Tischler, M. B., Driscoll, J. T., Cauffman, M. G., and Freedman, C. J., "Study of Bearingless Main Rotor Dynamics from Frequency-Response Wind Tunnel Test Data," *Proceedings of the AHS Aeromechanics Specialists Conference* (San Francisco, CA), American Helicoper Society, Alexandria, VA, 1994, pp. 6.3-1–6.3-26.

[3]Arnold, U. T. P., Keller, J. D., and Curtiss, H. C., "The Effect of Inflow Models on the Dynamic Response of Helicopters," *Proceedings of the 21st European Rotorcraft Forum* (St. Petersburg, Russia), 1995, pp. VII-8.1–VII.8-13.

[4]Rosen, A., and Isser, A., "A New Model of Rotor Dynamics During Pitch and Roll of a Hovering Helicopter," *Journal of the American Helicopter Society*, Vol. 40, No. 3, 1995, pp. 17–28.

[5]Takahashi, M. D., Fletcher, J. W., and Tischler, M. B., "Development of a Model Following Control Law for Inflight Simulation Using Analytical and Identified Models," *Proceedings of the 51st Annual Forum of the American Helicopter Society* (Fort Worth, TX), American Helicopter Society, Alexandria, VA, 1995, pp. 343–356.

[6]Leishman, J. G., and Nguyen, K. Q., "State Space Representation of Unsteady Airfoil Behavior," *AIAA Journal*, Vol. 28, No. 5, 1990, pp. 836–844.

[7]Celi, R., "Hingeless Rotor Dynamics in Coordinated Turns," *Journal of the American Helicopter Society*, Vol. 36, No. 4, 1991, pp. 39–47.

[8]Peters, D. A., and Barwey, B., "A General Theory of Rotorcraft Trim," *Proceedings of the AIAA/ASME/ASCE/AHS/ASC 36th Structures, Structural Dynamics, and Materials Conference* (New Orleans, LA), AIAA, Washington, DC, 1995, pp. 2558–2590.

[9]Peters, D. A., and Izadpanah, A. P., "Helicopter Trim by Periodic Shooting with Newton-Raphson Iteration," *Proceedings of the 37th Annual Forum of the American Helicopter Society* (New Orleans, LA), American Helicopter Society, Alexandria, VA, 1981, pp. 217–226.

[10]Subramanian, S., and Gaonkar, G. H., "Parallel Fast-Floquet Analysis of Trim and Stability for Large Helicopter Models," *U.S. Army Research Office 6th International Workshop on Dynamics and Aeroelastic Stability Modeling of Rotorcraft Systems* (Los Angeles, CA), 1995.

[11]Turnour, S. R., and Celi, R., "Modeling of Flexible Rotor Blades for Helicopter Flight Dynamics Application," *Journal of the American Helicopter Society*, Vol. 41, No. 1, 1996, pp. 52–66.

[12]Peters, D. A., and Cheng, J. H., "Correlation of Measured Induced Velocities with a Finite-State Wake Model," *Journal of the American Helicopter Society*, Vol. 36, No. 3, 1991, pp. 59–70.

[13]Kim, F. D., Celi, R., and Tischler, M. B., "High Order State Space Simulation Models of Helicopter Flight Mechanics," *Journal of the American Helicopter Society*, Vol. 38, No. 4, 1993, pp. 16–27.

[14]Kim, F. D., Celi, R., and Tischler, M. B., "Forward Flight Trim Calculation and Frequency Response Validation of a High-Order Helicopter Simulation Model," *Journal of Aircraft*, Vol. 30, No. 6, 1993, pp. 854–863.

[15]Chen, R. T. N., and Jeske, J. A., "Kinematic Properties of the Helicopter in Coordinated Turns," NASA TP 1773, April 1981.

[16]More, J. J., Garbow, B. S., and Hillstrom, K. E., "User's Guide for MINPACK-1," Argonne National Lab., Rept. ANL-80-74, Aug. 1980.

[17]Shampine, L. F., and Gordon, M. K., *Computer Solution of Ordinary Differential Equations—The Initial Value Problem*, W. H. Freeman and Company, San Francisco, CA, 1975.

[18]Turnour, S. R., "Flight Dynamic Simulation Modeling for Hingeless and Bearingless Rotor Helicopters," Ph.D. Dissertation, Dept. of Aerospace Engineering, Univ. of Maryland, College Park, MD, July 1996.